Electrostatic force method to determine flexure stiffness with an integrated fiber-optic displacement interferometer

Kumar Arumugam,[1, a)] Jonathan Cripe,[1, b)] Sven Schulze,[1, c)] Stephan Schlamminger,[1] and Gordon Shaw[1]
National Institute of Standards and Technology, Gaithersburg, USA

(*Electronic mail: gordon.shaw@nist.gov)

(Dated: 1 December 2025)

We have developed a miniature fused silica flexure-based reference spring which integrates a sphere-flat capacitive electrostatic actuator and a fiber optic displacement sensor to measure flexure stiffness as defined by Hooke's law. The experimental method can be adapted for measurement traceable to physical constants. A separate calibration using a reference mass validates the measurement. The measured stiffness values from these methods are (45.65 ± 0.84) $\mathrm{N\,m^{-1}}$ and (46.79 ± 0.93) $\mathrm{N\,m^{-1}}$, respectively. With a displacement measurement resolution of 40 pm, this reference spring can be used to calibrate forces as low as 2 nN. The instrument represents an important step towards providing a compact small mass and force reference with embedded metrology traceable to the International System of Units (SI). This method can be applied to a variety of measurements, including calibration of atomic force microscope (AFM), instrumented indentation, photon pressure force measurements, and of reference masses.

NOMENCLATURE

$\Delta\theta$	bubble level sensitivity
ε_0	vacuum permittivity
λ	laser wavelength
$\mathrm{d}C/\mathrm{d}z$	capacitance gradient
ν	Poisson's ratio
ω	oscillation frequency
ω_0	fundamental natural frequency
ω_d	damped natural frequency
σ	standard deviation
τ	decay time
ξ	damping ratio
B	flexure leaf width
C	capacitance
c_z	damping coefficient
D_y, D_z	distance between the flexure leafs in Y and Z axis
E	Elastic modulus
F	force
f_0	fundamental natural frequency in Hz
f_d	damped natural frequency in Hz
G	Rigidity modulus
g	local acceleration due to gravity
G_z	frequency response function
h	distance between the rod electrode plane and the sphere electrode center
I	electric current
k_x, k_y, k_z	flexure translation stiffness in X, Y and Z axis
k_Θ, k_Ψ, k_Φ	flexure rotation stiffnesses in X, Y and Z axis
$k_{z,e}$	flexure translation stiffness in Z axis determined by electrostatic method
$k_{z,m}$	flexure translation stiffness in Z axis determined by reference mass method
L	flexure leaf length
M	moment
m	reference mass
m_z	flexure modal mass
Q	quality factor
q	electric charge
r	sphere electrode radius
T	flexure leaf thickness
t	time
u	measurement uncertianty
V	voltage applied to electrodes
V_s	surface potential
V_{pd}	photodetector displacement response voltage
z	displacement

[a)] also at Joint Quantum Institute - University of Maryland, and Johns Hopkins University, USA
[b)] also at Laboratory for Physical Sciences, College Park, MD, USA
[c)] also at Technische Universität Ilmenau, Germany

I. INTRODUCTION

In recent years, particularly following the 2019 revision of the International System of Units (SI), electrostatic force compensation has been increasingly employed for the direct realization of forces traceable to physical constants. This approach has enabled high precision measurements such as the weighing of milligram masses and the measurement of photon pressure force to determine laser power. With this technique, milligram mass measurements reach measurement uncertainties less than 10 ng, an order of magnitude lower than conventional kilogram sub-division[1,2]. Additionally, measurements of photon momentum transfer forces (radiation pressure) have demonstrated repeatability within a few pN[3,4], with forces as low in the nN and sub-nN range from 1 W and 7 mW lasers respectively. Furthermore, electrostatic force balances have been employed to provide SI-traceable calibrations of reference springs used in measuring forces applied by atomic force microscopes and nanoindenters[5–9]. These springs are typically designed as cantilever beams[10], with their stiffness or the sensitivity of an integrated sensor determined by applying a known force via the balance and measuring the corresponding displacement or sensor output. The literature[11–15] also includes reference springs of various geometries that incorporate active components for internal metrology or active force control.

A common thread among these studies is an initial calibration using a separate reference device before deployment to the end user. Consequently, the user's calibration relies on a transfer artifact. Alternatively, a known electrostatic force can be applied directly to a sensor in an instrument, and that instrument's internal measurement capabilities can be used to measure the response[12,16,17]. Our work presents the development of a self-calibrating reference spring designed to be more versatile than previous works (see Table I, allowing it to be utilized in various contexts where precise measurement of small masses and forces is required and auxiliary metrology may not be present. To determine its stiffness, the instrument incorporates an electrostatic actuator that applies forces in the micronewton range and a fiber-optic Fabry-Perot interferometer for measuring displacements at the nanometer level. The spring is designed as a parallelogram flexure made of fused silica (Fig.1) measuring 13.4 mm×2 mm×2 mm. fabricated monolithically by femtosecond laser-assisted chemical etching[18,19]. The compact size of our instrument facilitates the manual assembly of the electrostatic actuator and fiber-optic sensor, enabling performance studies and validation through comparisons with results obtained by applying gravitational force using a reference mass.

II. PRINCIPLE OF OPERATION

The electrostatic force, F, applied to the flexure is generated by an electrode pair consisting of a 0.5 mm brass sphere, epoxied to the moving flexure, and a fixed stainless steel rod. When a voltage is applied across the electrodes, the resulting electrostatic force pulls the flexure toward the fixed electrode, reducing the electrode gap by distance z, and increasing the capacitance, C, between the electrodes. The measured voltage, V, is the sum of the potential drop in the gap between the electrodes, and a surface or contact potential, as described further below. Displacement is measured using a fiber- Fabry-Perot laser interferometer positioned adjacent to the electrodes.

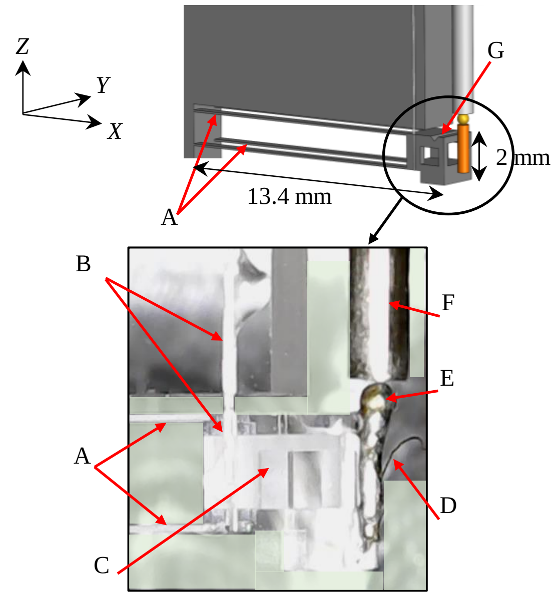

FIG. 1. Assembly showing: the parallelogram mechanism made of fused silica with its flexure leafs (A); a single-mode fiber-optic interferometer cavity (B), with one fiber end attached to the flexure platform (C) for measuring flexure displacement; sphere (E) and rod (F) electrodes forming the electrostatic actuator, with the sphere attached to the flexure platform; a gold wire (D) for electrically ground the sphere; and a V groove (G) for loading the reference mass wire.

$$F = \frac{1}{2}\frac{\mathrm{d}C}{\mathrm{d}z}V^2, \tag{1}$$

where $\mathrm{d}C/\mathrm{d}z$ is the capacitance gradient. From Hooke's law, the flexure stiffness is

$$k_{z,e} = \frac{F}{z}. \tag{2}$$

As an alternative method to determine the flexure stiffness, a reference mass (m) is loaded on the flexure to cause a displacement,

$$k_{z,m} = -\frac{mg}{z}, \tag{3}$$

where g is the local gravitational acceleration, and the negative sign indicates that the electrostatic and gravitational forces are in opposite directions for our device.

III. EXPERIMENTAL APPARATUS

Fig. 1 shows a cleaved fiber mirror and spherical electrode mounted to the end of the flexure. Another cleaved optical

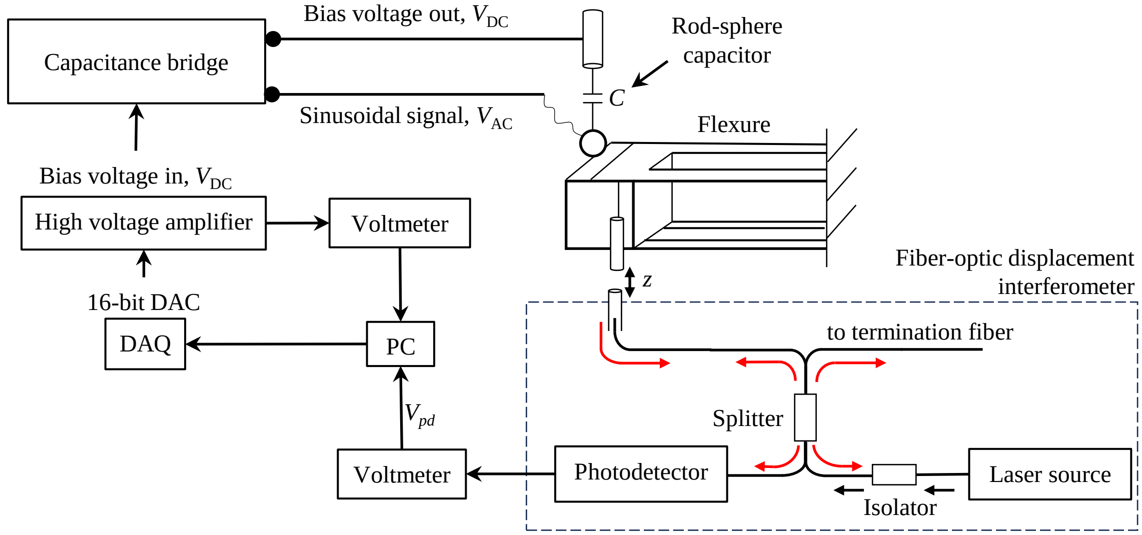

FIG. 2. Schematic of the experimental setup showing the flexure, capacitance bridge, high voltage amplifier supplying the electrodes through the bridge, fiber-optic arrangement to measure displacement, voltmeters to measure the interferometer photodetector intensity and the voltage applied to the electrodes, and the data acquisition[20] device with a 16-bit digital to analog converter.

TABLE I. Comparison of our device to similar studies reported in literature. Our work employs a sphere–rod capacitor, a sphere–coaxial wire capacitor is used in[12], and the others use plate–plate capacitors.

Device	Material	Fabrication method	Cross-sectional area (mm × mm)	Stiffness (N/m)	Resonant frequency (Hz)	Displacement (μm)	Electrostatic force applied (μN)	Measurement uncertainty (%)
Torsional spring, [15]	Be-Cu	Photochemical milling	15 × 15	0.13	22.5	30	3.9	3.5
Electrical Nanobalance[11]	Poly-Si	chemical vapor deposition	1 × 0.5	0.2	4300	0.4	0.08	5
Colloidal probe 6[12]	Si	Photolithography	0.14 × 0.018	0.35	10900	0.14	0.04	10
Nanoforce actuator[13]	Mono-Si	Bonding and deep reactive ion etching	2.5 × 2.5	13	1740	6	70	0.4
Force balance[21]	Cu-Be	Wire-electro discharge machining	75 × 20	20	10.9	4	80	1
This work	fused silica	Laser asisted chemical etching	13.4 × 2	46	313	0.1	4	4

fiber mounted on the fixed glass substrate acts as the second reflector of the low finesse Fabry-Perot interferometer. This measures flexure displacement due to either electrostatic force, or gravitational force from a reference mass. A flat electrode forms a capacitor with the spherical electrode, enabling electrostatic force generation via a DC bias voltage applied through a capacitance bridge. Fig. 2 shows the schematic of the overall opto-electro-mechanical setup.

A. Flexure mechanism

The parallelogram flexure mechanism enables a single-degree-of-freedom rectilinear motion. It comprises four leaf springs (length $L = 11.4$ mm, width $B = 0.5$ mm, and thickness $T = 80$ μm) made of fused silica chosen for low thermal expansion and compatibility with laser-assisted chemical etching fabrication. V-grooves on the side and top of the flexure platform align the optical fibers and provide a stable location for the reference mass, respectively. Table II lists the analytically calculated flexure stiffnesses in six-axes, assuming an elas-

TABLE II. Linear and angular stiffness of the flexure for an applied force and moment respectively in six degrees of freedom[23].

Analytical expression	Analytical result	FEA result	Unit
$k_x = \frac{4EBT}{L}$	1	0.93	$\mathrm{MN\,m^{-1}}$
$k_y = \frac{4ETB^3}{L^3}$	1.92	1.6	$\mathrm{kN\,m^{-1}}$
$k_z = \frac{4EBT^3}{L^3}$	49.21	49.28	$\mathrm{N\,m^{-1}}$
$k_\Theta = \sqrt{2}D_y^2\left(\frac{EBT^3}{L^3}+\frac{ETB^3}{2L^3}\right) + \frac{4GBT^3}{3(L-0.4B)}$	0.0017	0.0018	$\mathrm{N\,m\,rad^{-1}}$
$k_\Psi = \frac{EBT(D_z-T)^2}{L}$	0.45	0.58	$\mathrm{N\,m\,rad^{-1}}$
$k_\Phi = \frac{EB^3T}{3L} + \frac{EBTD_y^2}{L}$	0.58	0.58	$\mathrm{N\,m\,rad^{-1}}$

tic modulus $E = 70\,\mathrm{GPa}$, shear modulus $G = 0.5E(1+\nu)^{-1}$, and Poisson ratio $\nu = 0.15$. The distances between the neutral axis of the leafs in the y and z axes are $D_y = 1.5$ mm anf $D_z = 1.42$ mm. Finite element analysis (FEA) simulations were performed to compare analytical stiffness estimates. Linear stiffness k_x, k_y, and k_z were determined by applying forces $F_x = 1\,\mathrm{N}$, $F_y = 1\,\mathrm{N}$ and $F_z = 1\,\mathrm{mN}$ on the flexure platform and recording its displacements in x, y and z axes, respectively. Angular stiffness k_Θ, k_Ψ, and k_Φ were determined by applying moments $M_x = 1\times10^{-4}\,\mathrm{N\,m}$, $M_y = 1\times10^{-3}\,\mathrm{N\,m}$, and $M_z = 1\times10^{-3}\,\mathrm{N\,m}$ to record rotations about the x, y, and z axes, respectively. Flexures manufactured by laser-assisted chemical etching are reported to withstand stresses over 1 GPa[22], exceeding fused silica's typical tensile strength of 160 MPa. FEA shows a stress of 0.7 GPa on the flexure leafs under 100 mN (four orders of magnitude larger than the forces used in this study) causing a 2 mm deflection.

The equation of motion of the fundamental mode of the flexure is given by

$$m_z\frac{\mathrm{d}^2z}{\mathrm{d}t^2} + c_z\frac{\mathrm{d}z}{\mathrm{d}t} + k_z z = F_z, \tag{4}$$

where F_z is an external force in z direction, m_z is the modal mass, c_z is damping coefficient and t is time. Abbreviating

$$\omega_0^2 \equiv (2\pi f_0)^2 = \frac{k_z}{m_z} \text{ and } \xi = \frac{c_z}{2m_z\omega_0}, \tag{5}$$

where ω_0 is fundamental natural frequency and ξ is damping ratio. The equation of motion is written as

$$\frac{\mathrm{d}^2z}{\mathrm{d}t^2} + 2\xi\omega_0\frac{\mathrm{d}z}{\mathrm{d}t} + \omega_0^2 z = \frac{1}{m_z}F_z \tag{6}$$

The external force $F_z(t) = \mathrm{Re}\left(F_a\exp(j\omega t)\right)$, produces a displacement $z(t) = \mathrm{Re}\left(z_a\exp(j\omega t)\right)$, where the relationship between z_a and F_a is determined by the complex frequency response function

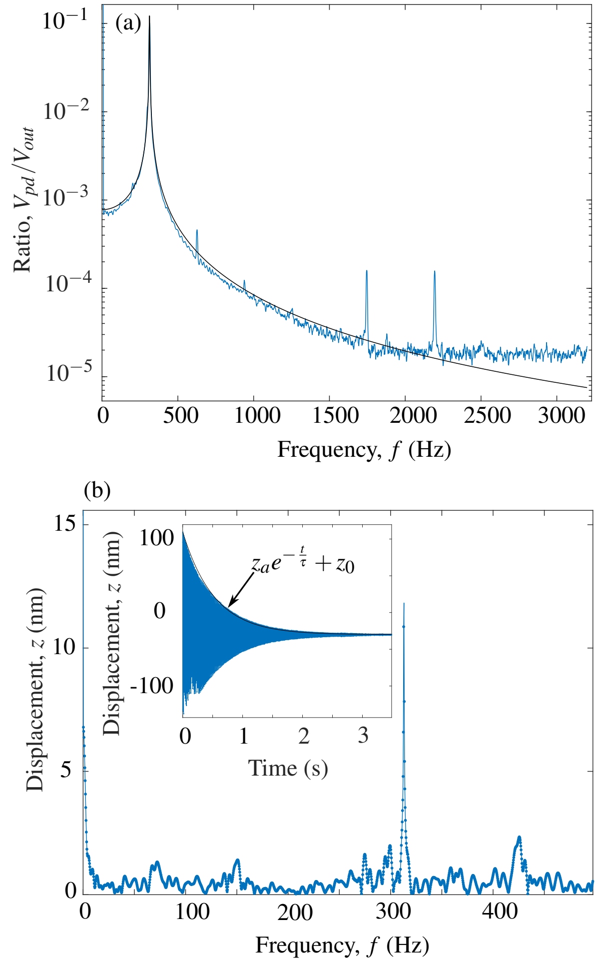

FIG. 3. Dynamic response of the system; (a) frequency response function produced using a dynamic signal analyzer showing the resonance frequency and multiple harmonics, (b) Fourier transform of the step response signal shown in the inset used to calculate the resonance frequency at 313 Hz. The black line in (a) is a fit to $V_{pd}/V_{out} \propto G_z(\omega)$.

$$G_z(\omega) = \frac{z_a}{F_a} = \frac{1}{k_z}\frac{1}{1-\frac{\omega^2}{\omega_0^2}+2j\xi\frac{\omega}{\omega_0}}. \tag{7}$$

For completion, it is noted that the homogeneous solution to Eq. 4 is a damped harmonic motion with the natural frequency of f_n given by

$$\omega_d \equiv 2\pi f_d = \omega_0\sqrt{1-\xi^2}. \tag{8}$$

The decay time τ and the quality factor Q of the oscillator are given by

$$\tau = \frac{1}{\omega_0\xi} \text{ and } Q = \frac{1}{2\xi}, \tag{9}$$

respectively. The flexure dynamic response was measured using a sinusoidal frequency sweep with a dynamic signal analyzer[24]. The voltage output V_{out} from the analyzer is connected to the electrodes to apply force on the flexure. The displacement response voltage V_{pd} from the interferometer photo detector, which is for small displacements proportional to z (see section III C), is connected to the input of the analyzer. The ratio of these voltages, V_{pd}/V is shown in FIG. 3(a) along with a fit to Eq.(7) in black. From this, the fundamental resonant frequency and the damping ratio is determined to be $f_0 = (312.9 \pm 0.1)$ Hz and $\xi = (1.5 \pm 0.64) \times 10^{-3}$ respectively. As another approach, the experimental base is gently tapped (see Fig. 6(a)) to produce the impulse response shown in the inset of FIG. 3(b). An exponential fit is applied to this signal with amplitude $z_a = 140$ nm, decay rate time $\tau = 0.53$ s, offset $z_0 = -30$ nm. From the Fourier transform shown in FIG. 3(b), the resonant frequency is determined to be $f_d = (312.93 \pm 0.03)$ Hz. The damping ratio and the Q-factor of the system are given by $\xi = (8.3 \pm 0.4) \times 10^{-4}$ and $Q = 600 \pm 28$, respectively.

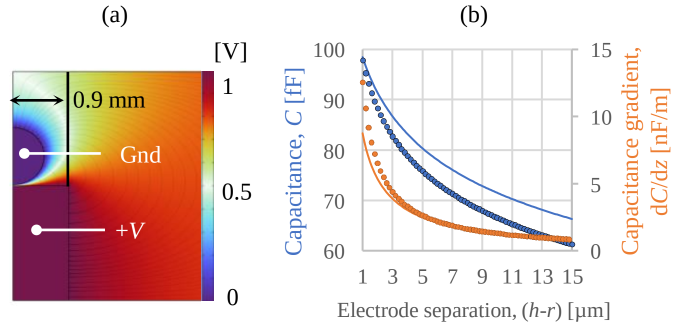

FIG. 4. Analytical model and a simulation estimating the capacitance of a sphere-flat electrode as a function of electrode separation; (a) COMSOL® simulation with color scale indicating the electric potential, and (b) results of the analytical model of capacitance and capacitance gradient shown in blue and orange solid lines, corresponding simulation results are given by the dots of the same.

B. Electrostatic actuator

The capacitor electrodes are a 0.5 mm diameter brass sphere and a 0.9 mm diameter stainless steel rod. The sphere is epoxied to the flexure (see FIG. 1) and soldered to a 25 μm diameter, 50 mm long gold-beryllium fine wire for electrical contact[25]. From the cantilever beam bending model, this wire's stiffness would not exceed $\mu\mathrm{N\,m^{-1}}$ level. The rod is attached to a five-axis parallel manipulator[26] to center it with respect to the sphere while monitoring using a camera. The end face of the rod was hand polished flat using sandpapers with grit size down to 2500 on a float glass. Surface topography of the end face measured using a Coherence scanning interferometer[27] reveal a convex curvature of 10 μm peak-to-valley with a surface roughness of 600 nm peak-to-valley. Use of a simple rod rather than a coaxial flat electrode[12] reduces the complexity in determining the capacitance gradient when a co-axial wire is used, as described in our previous study[28]. Other types of electrode pairs found in the literature include plate-plate[3,19,21,29] and concentric cylinders[4,30].

An analytical equation[31] for capacitance vs. electrode separation of a sphere against a planar surface is given by

$$C = 8\pi\varepsilon_0\sqrt{h^2-r^2}\sum_{n=0}^{\infty}\frac{e^{-(n+0.5)\gamma}}{1-e^{-(n+0.5)\gamma}} \tag{10}$$
$$\gamma = 2\ln\left(\frac{h+\sqrt{h^2-r^2}}{r}\right),$$

where h is the distance between the plane and center of the sphere, r is the sphere radius, and $\varepsilon_0 = 8.854 \times 10^{-12}\,\mathrm{F\,m^{-1}}$ is the vacuum permittivity. Using this equation, the capacitance and its gradient for an electrode separation from 1 μm to 15 μm evalutated through $n = 10$ are shown in FIG. 4(b). For comparison, FIG. 4(a) shows a COMSOL® FEM simulation with results plotted as solid lines in 4(b). The difference between the simulation and the theory can be attributed to the finite extent of the xy plane of the rod electrode which is assumed to be infinite in the theory. The initial electrode gap is also not known precisely, as it would be if the flexure and the actuator were manufactured monolithically[19]. From FIG. 4(b) and the experimentally measured nominal capacitance of 73 fF shown in FIG. 9(a), the electrode gap can be estimated to be 6 μm. However, the experimentally determined capacitance gradient is $1.09\,\mathrm{nF\,m^{-1}}$ as discussed in section IV A, corresponding to a larger electrode gap of 12 μm. As a precaution, to avoid electric arcing between the electrodes, we assumed the gap to be 6 μm, keep the applied voltage below 254 V and limit the electrical current in our experiments, as discussed in the following subsection. Studies[32,33] indicate for such a gap, the breakdown voltage would exceed 350 V.

C. Fiber-optic displacement interferometer

To measure the flexure displacement z, a fiber Fabry-Perot interferometer is employed using a laser source[34] containing a a built-in wavelength meter with ±10 pm accuracy. The laser output fiber connects to a single mode evanescent wave fiber coupler[35], selected for its low return loss[36], via an isolator. As shown in FIG. 1, the flat cleaved exit end of the coupler fiber is attached to the V-groove on the fixed base of the flexure, and a flat cleaved termination fiber of 2 mm long is attached to V-groove on the moving flexure platform. All fiber connections are fusion spliced to minimize loss. The two flat faces of the fibers form the mirrors of the low finesse Fabry-perot cavity. The cavity spacing is estimated to be less than 25 μm, by sweeping the laser wavelength λ by 50 nm to create a interferometric signal including a complete period[37]. A method for calibrating the interferometer intensity signal to displacement by sweeping the laser wavelength is demonstrated in previous studies[28,36–38]. However, this approach is subject to laser wavelength dependent intensity variation, spurious ripples at the intensity peak due to parasitic cavities, and the deviations in the theoretical fit near

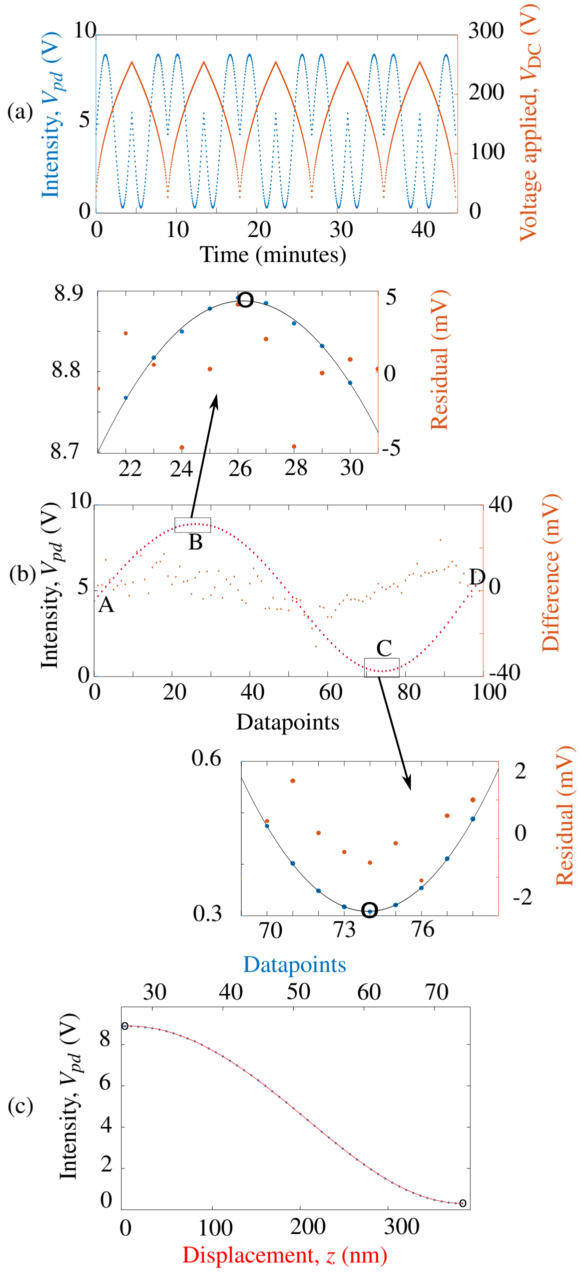

FIG. 5. Interferometric signal to measure displacement; (a) Intensity recorded by repeatedly reducing and increasing the cavity length by applying voltage to the electrostatic actuator, (b) average intensity of the repeats and its difference between the direction of cavity length change. Zoomed-in views show the 2$^{\text{nd}}$ order polynomial fit to the peak and the valley and its residual, (c) half cycle of the signal in (b), where the black circles indicate the peak and the valley points determined from the polynomial fit. Linear interpolation shown in red obtained from the calibration curve for displacement computation.

the peaks and the valleys of the signal. In our studies, the laser wavelength is kept constant at $\lambda = 1540$ nm or 1558 nm, and the interferometer signal is calibrated by varying the cavity length using the electrostatic actuator. Since the peak-to-valley of the signal corresponds to a displacement of $\lambda/4$ and the non-linearity of the flexure stiffness for a displacements under 1 µm is much smaller[39] than the measurement uncertainty goal of this work, we implemented a linear ramp in cavity length. As shown in FIG. 5(a), the linear ramp is achieved by applying a voltage from 0 V to 254 V in a square rooted manner (shown in orange) using the Kepco high voltage amplifier[40], see equations (1) and (2). This was repeated five times, producing an interferometric signal (shown in blue) slightly over a complete cycle with a peak-to-valley range of 8.9 V. The first half of the signal in each cycle corresponds to the decrease of electrode gap, while the second half represents the increase. These two signals are averaged and plotted as blue dots for decreasing electrode gap, red dots for increasing electrode gap in FIG. 5(b). The maximum difference between the up and down position ramps at the same applied voltage is less than 1 nm, attributed to system hysteresis. The zoomed-in views show the average of the blue and red data points near the peak and valley region. To obtain the calibration curve, instead of fitting the signal to a theoretical equation as done in prior works[28,36–38], we linearly interpolate between the measured data points. The difference between the interpolated points versus the points from a sine fit is only 2×10^{-6} V. The peak and valley of the signal are determined using a second order polynomial fit to the ten data points surrounding the peak and the valley respectively. The estimated peak and valley serve as the first and last data points of the half cycle plotted in blue dots as indicated by the black circles in FIG. 5(c). Given that the half cycle of the signal corresponds to a total displacement of $\lambda/4 = 385$ nm, and considering the position ramp linearity, the data points are linearly interpolated to produce the intensity versus displacement calibration curve shown in red.

The calibration discussed in this section uses a signal from a displacement of slightly over 770 nm, and the fringe region B to C is used to find its peak and valley, see FIG. 5(b). However, during the flexure stiffness measurement discussed in section IV A, the flexure was displaced only by 98 nm correspond to the region between A and B. Owing to the fringe symmetry[41], the calibration points from region B to C are used to calculate the displacement corresponding to the intensity change in region between A and B. The combined displacement calibration uncertainty due to non-linearity and variation in voltage increments, and surface potential effect is 0.9 %, which is listed in Table III.

D. Experimental environment

Measurements were conducted in a temperature-controlled environment at $(20\pm0.02)^{\circ}$C with the setup shown in FIG. 6(a) housed in an enclosure to reduce ambient air disturbances. The five-axis manipulator is used to to align the rod electrode, and the flexure assembly epoxied to an aluminum block is attached to a small breadboard. This breadboard mounted on a tip-tilt aligner[42] and XY stage to align the flexure V-groove with a reference mass. Another motorized[43] XY stage holds two flexible wire hooks to load and unload the

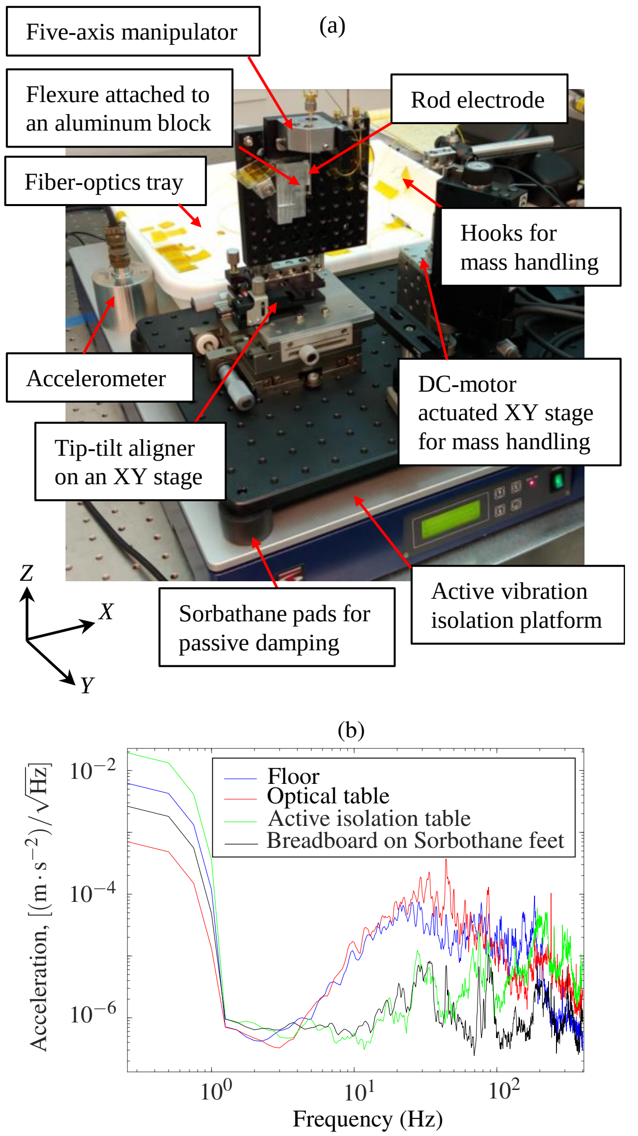

FIG. 6. Overall assembly; (a) equipment used for vibration isolation, mass handling for the validation study, also see FIG. 11(a). During the experiments an enclosure covers the setup to reduce ambient air disturbance, (b) vibration measured by the accelerometer shows the attenuation effect of passive and active damping in higher and lower frequencies respectively.

mass on the V-groove. All components are mounted on a larger breadboard with four Sorbathane feet[44] at the corners for passive vibration isolation, atop a piezoelectrically controlled active vibration isolation platform[45]. FIG. 6(b) shows the results of vibration measured using an accelerometer[46] placed on different stages of isolation.

E. Capacitance bridge

Our goal is to measure the capacitance gradient ($\mathrm{d}C/\mathrm{d}z$) when the electrode gap is linearly ramped to displace the flexure by applying a DC voltage V_{DC} to the rod electrode. However, the capacitance measurement requires an application of AC voltage $V_{\mathrm{AC}} = V_a \cos(\omega t)$ to the sphere electrode, consequently oscillating the flexure. Due to the flexure dynamics, the measured capacitance changes as a function of the capacitance bridge excitation frequency ω. This subsection discusses the theory and the mitigation of this effect. The capacitance bridge[47] utilizes co-axial cables with their shields reaching as close as possible to the electrodes to minimize stray capacitance. For the spherical electrode, the shielding ends near the fine gold wire soldered to the sphere. To minimize capacitive coupling between the electrodes and the aluminum block supporting the flexure, the block is connected to the bridge ground. The voltage difference between sphere and rod is given by

$$V = V_{\mathrm{DC}} + V_a \cos(\omega t), \tag{11}$$

where the bridge applies an AC voltage to the sphere. A DC bias voltage V_{DC} is applied incrementally to the rod ranging from 0 V to 91 V shown as black data points in FIG. 7 (a). This linearly increases the electrostatic force, and thus linearly decreases the electrode gap, since the force depends on V^2 according to Eq. (1) which is

$$\begin{aligned} V^2 &= V_{\mathrm{DC}}^2 + 2V_{\mathrm{DC}}V_a\cos(\omega t) + {V_a}^2\cos^2(\omega t) \\ &= V_{\mathrm{DC}}^2 + \frac{V_a^2}{2} + 2V_{\mathrm{DC}}V_a\cos(\omega t) + \frac{V_a^2}{2}\cos(2\omega t), \end{aligned} \tag{12}$$

The first two terms produce a force that is constant in time (DC), resulting in a displacement given by

$$z_{\mathrm{DC}} = \frac{1}{2k_z}\frac{\mathrm{d}C}{\mathrm{d}z}\left(V_{\mathrm{DC}}^2 + \frac{1}{2}V_{\mathrm{AC}}^2\right). \tag{13}$$

The third term produces a displacement at ω given by

$$z_{\mathrm{AC}} = \mathrm{Re}\left(G_z(\omega)\frac{1}{k_z}\frac{\mathrm{d}C}{\mathrm{d}z}V_{\mathrm{DC}}V_a\cos(\omega t)\right). \tag{14}$$

The 2-ω displacement can be calculated similarly but can be disregarded when calculating the capacitance measured by the bridge at ω. The current flow into a time-varying capacitor is given by the time derivative of the charge, which consists of two components.

$$I = \frac{\mathrm{d}q}{\mathrm{d}t} = C\frac{\mathrm{d}V}{\mathrm{d}t} + V\frac{\mathrm{d}C}{\mathrm{d}t} = C\frac{\mathrm{d}V}{\mathrm{d}t} + V\frac{\mathrm{d}C}{\mathrm{d}z}\frac{\mathrm{d}z}{\mathrm{d}t}. \tag{15}$$

The capacitance variation due to the DC displacement is given by the first-order Taylor series approximation as

$$C \approx C_0 + \frac{\mathrm{d}C}{\mathrm{d}z}z_{\mathrm{DC}}, \tag{16}$$

where, C_0 is the capacitance at the initial electrode gap. Furthermore, taking the time derivative of Eq. (14) for $\mathrm{d}z/\mathrm{d}t$ gives,

$$\begin{aligned} I_\omega = {} & C_0\frac{\mathrm{d}V}{\mathrm{d}t} + \frac{1}{2k_z}\left(\frac{\mathrm{d}C}{\mathrm{d}z}\right)^2\left(V_{\mathrm{DC}}^2 + \frac{1}{2}V_{\mathrm{AC}}^2\right)\frac{\mathrm{d}V}{\mathrm{d}t} - \\ & V\frac{\mathrm{d}C}{\mathrm{d}z}\mathrm{Re}\left(G_z(\omega)\frac{\mathrm{d}C}{\mathrm{d}z}V_{\mathrm{DC}}V_a\omega\sin(\omega t)\right), \end{aligned} \tag{17}$$

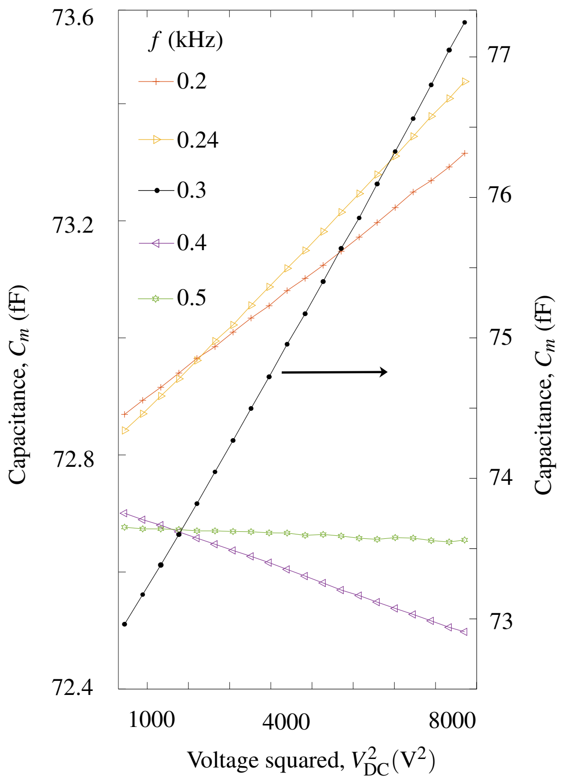

FIG. 7. Capacitance measured at different bridge excitation frequencies. The result at 300 Hz is plotted in the right-axis because of its larger magnitude.

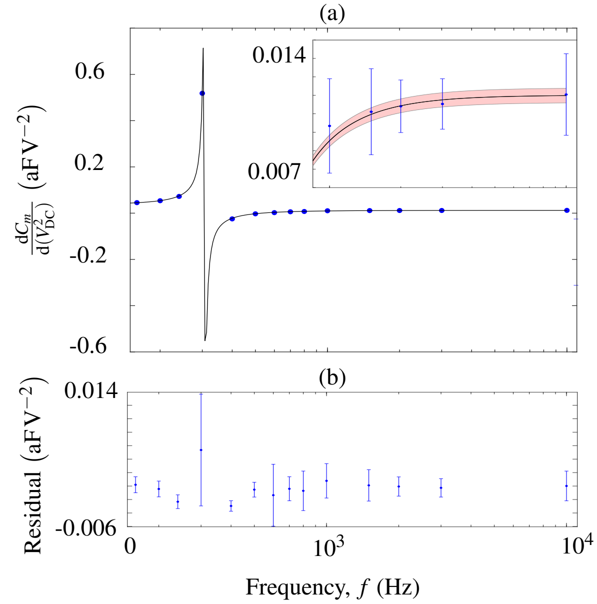

FIG. 8. Slope of the measured capacitance C_m versus the square of the voltage (a) plotted in blue dots as a function of different bridge excitation frequencies in log- scale. The black line is a fit to the model in Eq. (20). The inset shows the result from 1 kHz to 10 kHz frequency in linear scale with error bars indicating the standard deviation, and red shaded region representing the fit uncertainty, (b) residual from the fit and the measurement uncertainties shown as error bars.

where we have neglected terms that would produce a current at 2ω which are rejected by the capacitance bridge. Using Eq. (11) for V, we obtain $\mathrm{d}V/\mathrm{d}t = -V_a\omega\sin(\omega t)$. The measured capacitance, C_m reported by the bridge is given by

$$C_m = \frac{I_\omega}{-V_a\omega\sin(\omega t)}. \tag{18}$$

Substituting Eq. (17) in Eq. (18) results in

$$\begin{aligned} C_m \;=\; & C_0 + \frac{1}{2k_z}\left(\frac{\mathrm{d}C}{\mathrm{d}z}\right)^2\left(V_{\mathrm{DC}}^2 + \frac{1}{2}V_{\mathrm{AC}}^2\right) + \\ & \mathrm{Re}\left(G_z(\omega)\right)\left(\frac{\mathrm{d}C}{\mathrm{d}z}\right)^2 V_{\mathrm{DC}}^2, \end{aligned} \tag{19}$$

which is similar to the equation derived in a previous work[48]. During experiments, capacitance C_m is measured when the DC voltage V_{DC} applied to the rod is varied as a square-rooted ramp from 0 to 91 V. This test was repeated by varying the excitation frequency of V_{AC} applied to the sphere from f =160 Hz to 10 kHz. FIG. 7, for simplicity, only shows the measurement results near the resonant frequency at 300 Hz, and four adjacent frequencies. Each curve shown in FIG. 7 is an average of five cycles repeated at each frequency, and each data point is an average of 15 values measured for 12 s. The bridge is set to output a three-point averaged value, and five of these values are further averaged on the computer. The experiments use the maximum amplitude of V_{AC} 4 V RMS. One can observe a large capacitance change at 300 Hz near resonance, and an out-of-phase capacitance change at 400 Hz. These observations can be explained by Eq. (19) as will be discussed below. It can also be observed on the left side of the plot that the absolute value of C_m decreases (independent of the applied DC voltage) with an increase in the AC frequency, which is not accounted for by Eq. (19). We do not have an explanation for this phenomenon as no significant change in the electrode gap was observed. We believe this effect is caused by a small frequency-dependent bias in the capacitance measurement which remains the same as long as the frequency is not changed and, hence, drops out when the slope of C_m as a function of V_{DC}^2 is computed.

To verify Eq. (19), the slope of measured capacitance C_m versus V_{DC}^2 is plotted as a function of frequency in FIG. 8(a), as blue points. The model for this slope plotted as black curve is given by Eq. 20, which is derived from Eq. (19) by expanding its real part using Eq. (7).

$$\frac{\mathrm{d}C_m}{\mathrm{d}(V_{\mathrm{DC}}^2)} = \frac{1}{k_z}\left(\frac{\mathrm{d}C}{\mathrm{d}z}\right)^2\left(\frac{1}{2} + \frac{1-\omega^2/\omega_0^2}{\left(1-\frac{\omega^2}{\omega_0^2}\right)^2 + 4\xi^2\frac{\omega^2}{\omega_0^2}}\right). \tag{20}$$

The coefficients of the fit are $f_0 = (306.6 \pm 2.0)$ Hz, ξ = (6.8 $\pm$ 8.7) $\times10^{-3}$, and $(\mathrm{d}C/\mathrm{d}z)^2/k_z = (24 \pm 0.8)\times10^{-3}$ $\mathrm{aF\,V^{-2}}$.

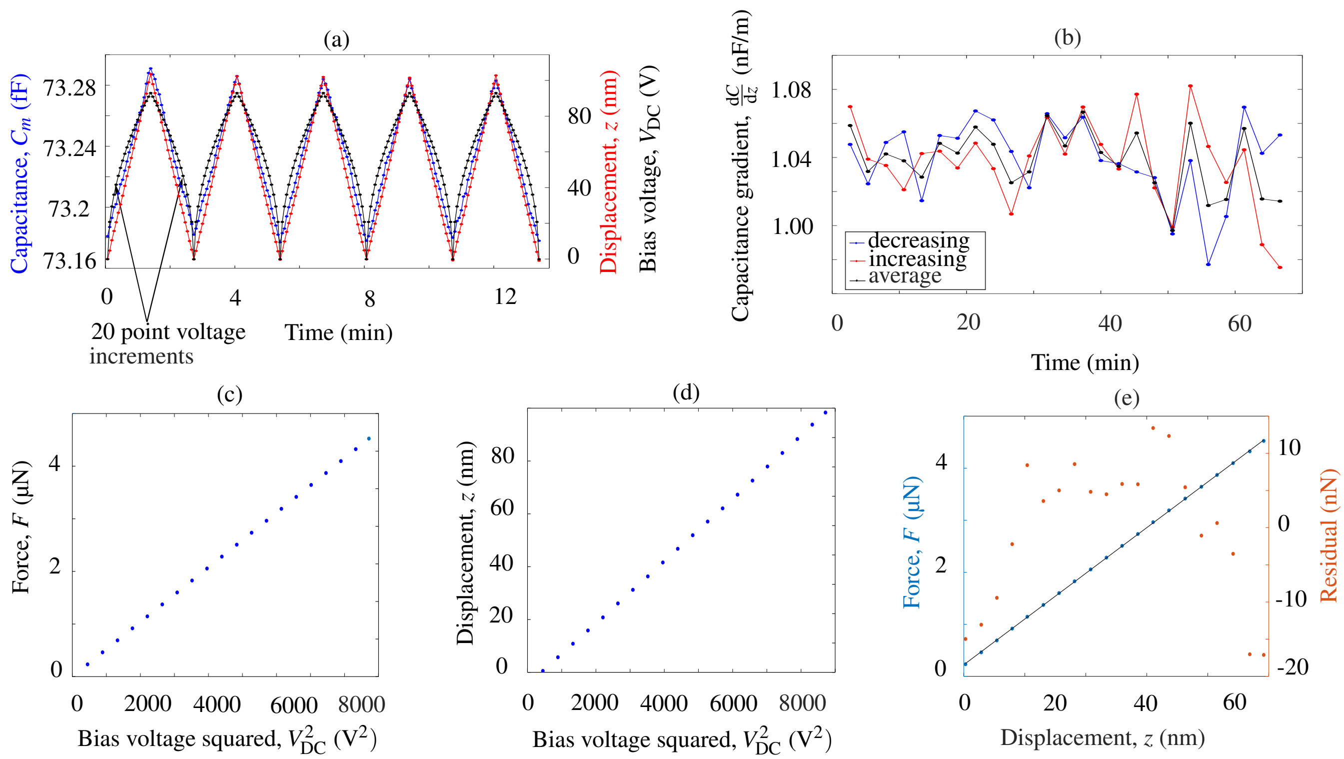

FIG. 9. Stiffness determination using the electrostatic force method; (a) voltage bias V_{DC} applied in a square root manner, measured capacitance and the displacement in the first 5 cycles, (b) capacitance gradient calculated by fitting a line to C_m vs. z measurement of the 25 cycles. Blue corresponds to the decreasing electrode gap when the voltage is ramped positively, and red vice versa, (c) electrostatic force average of 25 cycles calculated using equation (1), (d) displacement average of 25 cycles, (e) stiffness determined by fitting a line to F vs. z

.

For $\omega = 0$ and $\omega = \infty$, Eq. 20 evaluates to $3\left(\mathrm{d}C/\mathrm{d}z\right)^2/(2k_z)$ and $\left(\mathrm{d}C/\mathrm{d}z\right)^2/(2k_z)$. The inset in FIG.8(a) shows the data points and the fit for above 1 kHz, where it reaches its asymptote at 10 kHz, with the red shaded region representing the fit uncertainty. The measurement results discussed in section IV A uses the bridge excitation frequency of 2 kHz which still experience a frequency dependent variation as show in the inset of FIG. 8(a). To mitigate this, since the measured capacitance gradient is free of frequency dependent variation at 10 kHz, and it is 4.63 % higher than at 2 kHz, it is applied as a correction in section IV A. The uncertainty in this correction is determined using the uncertainties of the fit coefficients f_0 and ξ to be 0.06 %.

In summary, the capacitance bridge does not just report the capacitance due to the gap between the electrodes; it also gently excites the flexure while performing this measurement. Near the resonance, this excitation causes extra motion that the bridge interprets as a change in capacitance, which artificially steepens the measured slope. Far above resonance, the resonator cannot follow the excitation, so the measurement reflects the true geometric capacitance gradient. By mapping how the slope changes with frequency and fitting it to a simple mechanical response model, we can determine the real gradient and apply the appropriate correction when operating at 2 kHz. In short, the bridge measurement is a coupled electromechanical readout, and the frequency dependence tells us how much the dynamics inflate the apparent capacitance gradient.

IV. RESULTS

The following sections describe the procedure and results of the flexure stiffness determination by applying forces of similar magnitude using (A) electrostatic force method, and (B) mass loading method. For summary, see FIG. 10.

A. Stiffness measurement using the electrostatic force method

This section describes the experimental procedure and data analysis for determining flexure stiffness using the electrostatic force method. FIG. 9(a) shows the applied voltage V_{DC} using a Tegam[49] high voltage amplifier, measured capacitance C_m, and the displacement z of the first 5 cycles of a 25-cycle measurement lasting about an hour. Each data point is averaged for 1.6 ms and collected at 4-second intervals. During each cycle, the voltage V_{DC} was square root ramped up and down in increments of 20 voltage values between 0 and 93 V. Capacitance is plotted against displacement and a line (not shown) is fit to the data to calculate the capacitance gradient $\mathrm{d}C/\mathrm{d}z$ shown in FIG. 9(b). The blue data points corresponds to decreasing electrode gap for the positive voltage ramp, red

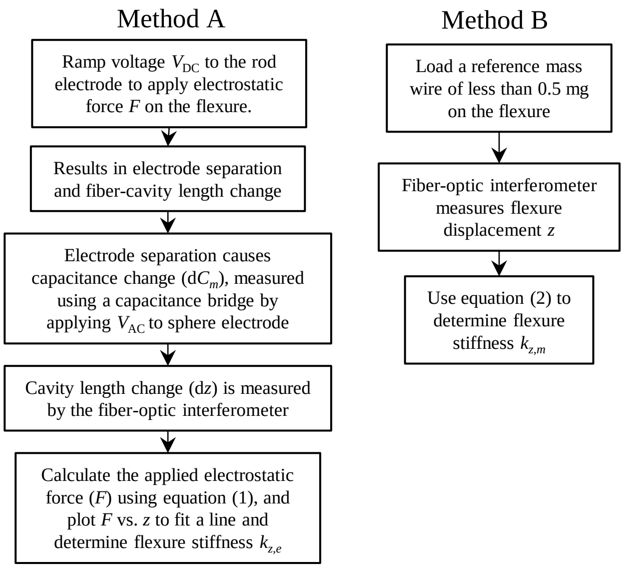

FIG. 10. A flow chart summarizing the experimental procedure to determine flexure stiffness using electrostatic force method (A), and reference mass method (B).

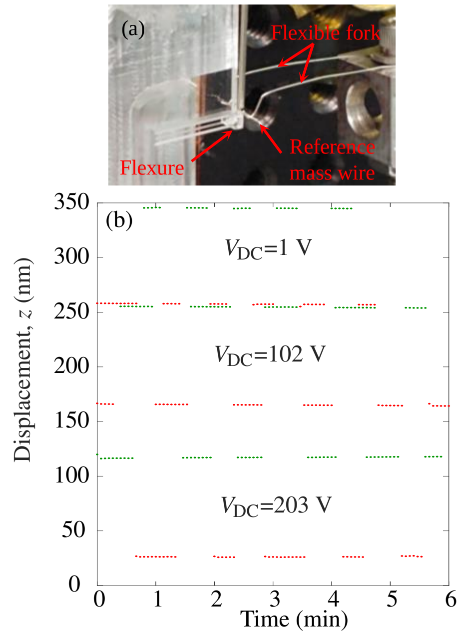

FIG. 11. Stiffness determination using the reference mass; (a) experimental setup showing the mass held in a flexible fork with hook ends to load and unload it on the flexure V-groove, (b) measured flexure displacement when the mass is loaded (green) and unloaded (red). The electrode gap is varied by supplying three different voltage values V_{DC} to the electrodes to operate at different regions of the interferometer calibration curve shown in FIG. 5(d).

is vice versa, and black is the average of the two measured to be (1.038 ± 0.018) nF m^{-1}. After applying the 4.63 % correction discussed at the end of section III E, this value becomes (1.086 ± 0.019) nF m^{-1}. The applied force F calculated using equation (1 and 12) is averaged for the 25 cycles, and plotted as a function of V_{DC}^2 in FIG. 9(c). The corresponding displacement is plotted in FIG. 9(D). To calculate F, the fixed offset force due to $V_a^2/2$ term and the dynamic force due to ω and 2ω terms in equation (12) are ignored, and only the V_{DC} term varied during the measurement are considered. Also, 0.4 V was subtracted from the measured V_{DC} to account for the surface potential discussed in Appendix IX A. To determine the flexure stiffness using equation (2), the force is plotted against the displacement as blue points on the left axis of FIG. 9(e). A line is fit to to this data to determine the stiffness of the flexure to be $k_{z,e} = (45.65 \pm 0.84)$ N m^{-1}. Without correcting for the surface potential, the determined stiffness was 0.7 % higher. The measured stiffness varied by 0.6 % between this measurement and another taken on an adjacent day. To indicate the non-linearity in stiffness determination, the residual from the line fit is plotted as orange points on the right axis of FIG. 9(e). The magnitude of non-linearity is obtained by dividing the 30 nN residual by the nominal displacement range of 98 nm to be 0.3 N m^{-1}.

B. Stiffness measurement using a reference mass

To determine the flexure stiffness using Eq. (3), a 99 % aluminum-silicon reference mass wire $m = (0.4258 \pm 0.0005)$ mg[50] was handled with a 0.5 mm diameter flexible stainless steel wire hooks to prevent flexure damage (FIG. 11(a)). The mass was loaded and unloaded five times to record flexure displacement z shown in FIG. 11(b). To cover the full range of the interferometer calibration curve shown in FIG. 5, measurements were taken at three electrode gaps by applying voltages V_{DC} = 1 V, 102 V, and 203 V with green and red data points indicating loaded and unloaded states, respectively. Each data point represents a 1.6 s average recorded every 6 s. To remove drift, two separate lines were fit to the loaded and unloaded states, resulting in 87.34 nm, 89.42 nm, and 90.86 nm. Using the average displacement (89.21 ± 1.77) nm in Eq. (2), flexure stiffness is determined to be $k_{z,m} = (46.79 \pm 0.93)$ N m^{-1}.

V. UNCERTAINTY EVALUATION

TABLE III lists the factors contributing to the uncertainty in flexure stiffness measurement. Both electrostatic and mass-based methods use the interferometric displacement sensor, so the accuracy of laser wavelength, bidirectional repeatability (1 nm / 385 nm = 0.26 %), shown in FIG. 5(b), as well as the digital voltmeter's (DVM) accuracy and resolution measuring intensity impacts both methods. To minimize power supply noise, each intensity measurement was averaged for ten power line cycles (10 NPLC, 1.66 ms) using the voltmeter. Consequently, the measurement resolution determined via Allan deviation is 2 mV, see FIG. 12. For the nominal operating point of 4.45 V in the signal shown in FIG. 5(c), the displacement measurement resolution is 0.045 %.

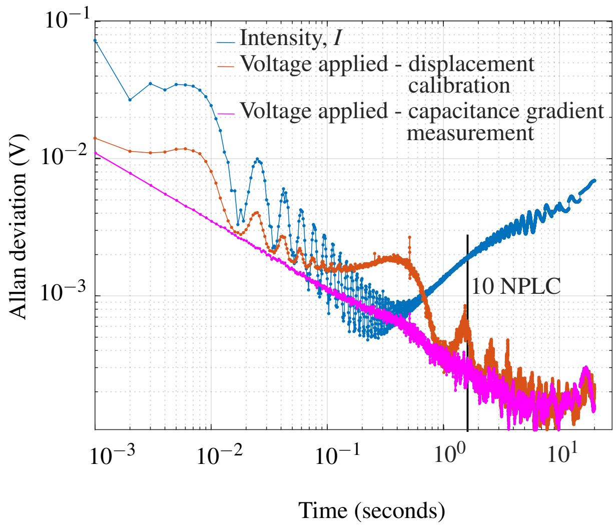

FIG. 12. Allan deviation of the interferometer intensity and the voltage applied to the electrodes. The raw signals were recorded for 1 minute at 1 ms sample rate to calculate the Allan deviation. The vertical black line indicates the 1.66 s averaging time (ten power line cycles, NPLC) used in the experiments. The minimum noise that can be obtained from the interferometer intensity is given by the Allan deviation minimum around 1 mV. Using this and the local slope (approximately 40 nm V^{-1}) of the sensitive mid region of the interference signal shown in FIG. 5(c), the resolution of the displacement computation is determined to be 40 pm.

TABLE III. Factors contributing to the measurement uncertainty (1-σ standard deviation)

Variable	Component	Rel. unc., u
Displacement, z	λ accuracy	6.5×10^{-6}
	bidirec. repeatability	2.6×10^{-3}
	DVM accuracy	3.5×10^{-5}
	Allan deviation	4.5×10^{-4}
	voltage non-linearity	9×10^{-3}
	linear interpolation	2×10^{-6}
	Electrostatic force method	
Capacitance, C	σ_{C_m}	1.75×10^{-2}
	bridge accuracy	2×10^{-5}
	freq. dependence correction	6×10^{-4}
Displacement, z	σ_z	5×10^{-3}
	photodiode drift and gain	1.5×10^{-3}
Applied voltage, V_{DC}	Allan dev. $\sigma_{V_{\mathrm{DC}}}$	5.3×10^{-4}
Surface potential, V_s	σ_{V_s}	1.75×10^{-4}
	Reference mass method	
Reference mass, m	σ_m	1.2×10^{-3}
	corner loading	2.6×10^{-2}
	buoyant force	4×10^{-4}
Flexure orientation[37]	$\tan\theta\cdot\Delta\theta$	5×10^{-5}
Accel. gravity	g =9.801 m s^{-2}	2×10^{-6}
Displacement, z	intensity dependence	2×10^{-2}
	σ_z	4.2×10^{-3}
Electrostatic force method: Total		2.8×10^{-2}
Reference mass method: Total		3.8×10^{-2}

In the electrostatic force method, the standard deviation of capacitance measurement is $\sigma_{C_m} = 1.27$ fF and the maximum standard deviation of the displacement measurement shown in FIG.9(d) is σ_z = 0.6 nm. For the nominal capacitance of 73 fF and the displacement of 98 nm shown in FIG. 9(a), it is σ_{C_m}= 1.75 % and σ_z = 0.5 % respectively. The interferometer intensity to displacement calibration shown in FIG. 5 was performed both before and after the capacitance gradient measurements shown in FIG. 9. The difference in the determined stiffness using the one or the other calibration curve is 0.15 %, accounting for the any drift and gain change in the photodiode. Uncertainty in frequency dependent correction of the measured capacitance discussed at the end of section III E is 0.06 %. From FIG. 12, the Allan deviation in measuring the applied voltage during capacitance gradient measurement is 0.3 mV. This corresponds to a relative uncertainty in the calculated stiffness of 0.53 %. Uncertainty in the correction of 0.4 V static potential is $\sigma_{V_s} = 0.01$ V, see the end of section IV A and Appendix IX A. This changes the calculated stiffness by 1.75×10^{-4}. By propagating all the measurement uncertainties through equations (1 and 2), the combined stiffness measurement uncertainty for the electrostatic method $u_{k_{z,e}}$ is evaluated to be 2.8 %.

$$u_{k_{z,e}} = \sqrt{(-2u_z)^2 + u_{C_m}^2 + (2u_{V_{\mathrm{DC}}})^2 + (2u_{V_s})^2} \quad (21)$$

The reference mass wire used in the mass-based method was measured using a microbalance with a standard deviation of $\sigma_m = 0.5$ µg (0.12 % of the reference mass value). The buoyant force experienced by the mass is 0.04 % of its weight. Prior to loading the mass on the flexure, a bubble level with a sensitivity of $\Delta\theta = 5$ mrad mm^{-1} is used to align the flexure to local gravity. The bubble level was placed on a microscope slide attached to the bottom of the aluminum block on which the flexure is mounted, see FIG. 6(a). The machining angular tolerance of the aluminum block is conservatively assumed to be $\theta = 10$ mrad. This alignment contributes to an uncertainty of 5×10^{-5}. During loading, the reference mass wire will stay on the flexure v-groove until its center of mass goes beyond the platform width ($\Delta y = \pm 1$ mm). Since the angular flexure stiffness in x axis is k_Θ =0.0018 N m rad^{-1} (see TABLE II), the flexure platform would rotate by 2.3 µrad. Since the optical fiber is attached to the V-groove 1 mm away from the XZ plane cross-section, this results in an abbe error of 2.3 nm, which is 2.6 % of the average displacement of 89 nm as discussed in section IV B. As shown in FIG. 11(b), the computed displacement during the mass loading varies by 2 % at different regions of the interferometric calibration curve shown in FIG. 5(d), with the standard deviation of σ_z is 0.42 % at each region. The combined stiffness measurement uncertainty using the reference mass is $u_{k_{z,m}} = 3.8$ %.

VI. DISCUSSION

The ultimate goal of this work is to develop compact and robust reference mass and force sensors. While miniaturizing techniques used in larger-scale instrumentation, some performance compromises are inevitable. The measurement uncertainty in this study, though comparable to similar past measurements using direct micro-scale capacitance techniques[12,17] is higher than that of larger electrostatic force balance systems[1,3,21]. The primary contributors to measurement uncertainty in the comparisons undertaken in this study are the capacitance measurement, corner loading during the mass calibration, and the fiber optic displacement measurement.

All of these challenges can be addressed with design modifications. For instance, the capacitor could be modified by applying a conductive indium-tin-oxide coating on platform to create a flat electrode[19]. This would increase the surface area and capacitance, making the bridge resolution less critical. The fiber interferometer is assembled manually by gluing optical fibers into v-grooves on the flexure, presents some challenges with optical alignment[51]. Fiber mirrors are used because the surface roughness of flat cleaved fiber edges is typically in single-digit nanometer range[52], preserving the contrast of the interferometer signal. In contrast, the laser assisted chemical etching process produces edges with surface roughness in the tens of nanometers[22]. To use these edges directly as a target mirror, techniques such as annealing[53], laser polishing[54], and oxyhydrogen flame polishing[55] are shown to reduce the surface roughness to nanometer levels. To eliminate corner loading error, a sphere mass in a cone constraint etched on the flexure platform could be used instead of the wire mass in a V-groove constraint, as employed in this study. The laser-assisted chemical etching process allows for rapid iteration of these design changes. Additionally, creating these sensors from monolithic fused silica ensures that their calibrations remain stable over time, with previous sensors retaining their calibrated values over several years[56].

Based on the sensor's spring constant and the minimum displacement resolution from FIG. 12, the force resolution of the sensor is approximately 2 nN. From the flexure geometry, the increase in stiffness is estimated[39] to be less than 2 % for a travel of 100 µm, allowing for an usable force range up to 4 mN when employing a suitable method for measuring larger displacements with the fiber interferometer[38]. There are multiple possible applications for a compact reference mass and force sensor in this range. For instance, measuring photon pressure force from laser reflection[4,57,58] has been used to establish an equivalence between SI force and optical power. The sensor developed in this work could be applied to measure optical power as low as 1 W and as high as is practically feasible, limited by the size of a high-reflectivity mirror, which can be mounted on the flexure platform which is only a few mm in length. Calibration of nanomechanical properties measurement instrumentation such as Atomic Force Microsopes[59] and instrumented indenters[17,37] is also feasible in this force range. As demonstrated in the paper, the sensor can also function as a spring balance for mass artifacts. Its force range suggests potential applications for measuring from micrograms to nearly half a gram, provided that precautions are taken to prevent damage to the sensor.

VII. CONCLUSION

A miniature flexure-based reference spring with an integrated electrostatic actuator and a fiber-Fabry perot displacement interferometric sensor has been developed to use as a stiffness transfer artefact. The flexure stiffness determined from the electrostatic force by measuring the capacitance gradient and applied voltage to the electrodes was found to be $(45.65 \pm 0.84)\ \mathrm{N\,m^{-1}}$. Alternatively, as another means of force; a reference mass was loaded on the flexure, yielding a stiffness value of $(46.79 \pm 0.93)\ \mathrm{N\,m^{-1}}$. The evaluated measurement uncertainty of the two methods are 2.8 % and 3.8 % (k=1) respectively. The instrument is capable of measuring force in the range from 2 nN (limited by interferometer resolution) to 4 mN (limited by nonlinearity of the flexure mechanism) with further improvement possible in both range and uncertainty. The device demonstrates the feasibility of a compact small mass and force reference that can be deployed to potentially provide SI-traceable mass and force values to an end-point user.

ACKNOWLEDGEMENT

Author KA would like to thank Stuart Smith (University of North Carolina at Charlotte) and Dannis Brouwer (University of Twente) for the discussions on flexure stiffness equations shown in TABLE II. Special thanks to Simon Schäfer (The Technische Universität Ilmenau) for experimental assistance, and Yiliang Bao (National Institute of Standards and Technology, USA) for conducting surface topography measurements of the rod electrode.

DISCLAIMER

Certain commercial equipment, instruments, and materials are identified in this paper in order to specify the experimental procedure adequately. Such identification is not intended to imply recommendation or endorsement by the National Institute of Standards and Technology, nor is it intended to imply that the materials or equipment identified are necessarily the best available for the purpose.

VIII. REFERENCES

[1] G. A. Shaw, J. Stirling, J. A. Kramar, A. Moses, P. Abbott, R. Steiner, A. Koffman, J. R. Pratt, and Z. J. Kubarych, "Milligram mass metrology using an electrostatic force balance," Metrologia **53**, A86 (2016).

[2] K. Arumugam and G. Shaw, "Perspective on small mass and force measurements," Measurement Science and Technology **34**, 081002 (2023).

[3]V. Nesterov, M. Mueller, L. Frumin, and U. Brand, "A new facility to realize a nanonewton force standard based on electrostatic methods," Metrologia **46**, 277 (2009).
[4]G. A. Shaw, J. Stirling, J. Kramar, P. Williams, M. Spidell, and R. Mirin, "Comparison of electrostatic and photon pressure force references at the nanonewton level," Metrologia **56**, 025002 (2019).
[5]J. R. Pratt, D. T. Smith, D. B. Newell, J. A. Kramar, and E. Whitenton, "Progress toward système international d'unités traceable force metrology for nanomechanics," Journal of Materials Research **19**, 366–379 (2004).
[6]M.-S. Kim, J.-H. Choi, Y.-K. Park, and J.-H. Kim, "Atomic force microscope cantilever calibration device for quantified force metrology at micro- or nano-scale regime: the nano force calibrator (nfc)," Metrologia **43**, 389 (2006).
[7]V. Nesterov, O. Belai, D. Nies, S. Buetefisch, M. Mueller, T. Ahbe, D. Naparty, R. Popadic, and H. Wolff, "Si-traceable determination of the spring constant of a soft cantilever using the nanonewton force facility based on electrostatic methods," Metrologia **53**, 1031 (2016).
[8]S. V. Beekmans and D. Iannuzzi, "A metrological approach for the calibration of force transducers with interferometric readout," Surface Topography: Metrology and Properties **3**, 025004 (2015).
[9]Y. Tian, C. Zhou, F. Wang, J. Zhang, Z. Guo, and D. Zhang, "A novel method and system for calibrating the spring constant of atomic force microscope cantilever based on electromagnetic actuation," Review of Scientific Instruments **89**, 125119 (2018).
[10]R. S. Gates and J. R. Pratt, "Prototype cantilevers for SI-traceable nanonewton force calibration," Measurement Science and Technology **17**, 2852–2860 (2006).
[11]P. J. Cumpson and J. Hedley, "Accurate analytical measurements in the atomic force microscope: a microfabricated spring constant standard potentially traceable to the si," Nanotechnology **14**, 1279 (2003).
[12]K. H. Chung, G. A. Shaw, and J. R. Pratt, "Accurate noncontact calibration of colloidal probe sensitivities in atomic force microscopy," Review of Scientific Instruments **80**, 065107 (2009).
[13]S. Gao, Z. Zhang, Y. Wu, and K. Herrmann, "Towards quantitative determination of the spring constant of a scanning force microscope cantilever with a microelectromechanical nano-force actuator," Measurement Science and Technology **21**, 015103 (2009).
[14]J. Melcher, J. Stirling, F. G. Cervantes, J. R. Pratt, and G. A. Shaw, "A self-calibrating optomechanical force sensor with femtonewton resolution," Applied Physics Letters **105**, 233109 (2014).
[15]J. F. Portoles and P. J. Cumpson, "A compact torsional reference device for easy, accurate and traceable afm piconewton calibration," Nanotechnology **24**, 335706 (2013).
[16]U. Mohideen and A. Roy, "Precision measurement of the casimir force from 0.1 to $0.9\mu m$," Phys. Rev. Lett. **81**, 4549–4552 (1998).
[17]K.-H. Chung, S. Scholz, G. A. Shaw, J. A. Kramar, and J. R. Pratt, "SI traceable calibration of an instrumented indentation sensor spring constant using electrostatic force," Review of Scientific Instruments **79**, 095105 (2008).
[18]V. Tielen and Y. Bellouard, "Three-dimensional glass monolithic micro-flexure fabricated by femtosecond laser exposure and chemical etching," Micromachines **5**, 697–710 (2014).
[19]B. Lenssen and Y. Bellouard, "Optically transparent glass micro-actuator fabricated by femtosecond laser exposure and chemical etching," Applied Physics Letters **101**, 103503 (2012).
[20]USB-6212, National Instruments.
[21]S.-J. Chen and S.-S. Pan, "A force measurement system based on an electrostatic sensing and actuating technique for calibrating force in a micronewton range with a resolution of nanonewton scale," Measurement Science and Technology **22**, 045104 (2011).
[22]Y. Bellouard, "On the bending strength of fused silica flexures fabricated by ultrafast lasers," Opt. Mater. Express **1**, 816–831 (2011).
[23]S. T. Smith, B. M. Dannis, M. Nijenhuis, and K. Arumugam, "Flexures: elements of elastic mechanism design, second edition," Crc Press (forthcoming 2026).
[24]35670A, Dynamic signal analyzer, Hewlett Packard.
[25]99.99 % gold berryllium wire, California fine wire co.
[26]9016NF, five-Axis fiber positioner, Newport.
[27]NT1100, Coherence scanning intereromter, Wyco®.
[28]K. Arumugam, J. Cripe, S. Schulze, S. Schlamminger, and G. Shaw, "Stiffness measurement of a miniature glass flexure using the electrostatic force produced by sphere-coaxial wire electrodes," 34th Annual Meeting of American Society for Precision Engineering (2023).
[29]C. W. Jones and R. K. Leach, "Review of low force transfer artefact technologies." (2008).
[30]Y. Yamamoto, K. Fujita, and K. Fujii, "Si traceable small mass measurement using the voltage balance apparatus at nmij," (2018).
[31]C. Snow, "Formulas for computing capacitance and inductance," US Government Printing Office **544** (1954).
[32]A. Peschot, N. Bonifaci, O. Lesaint, C. Valadares, and C. Poulain, "Deviations from the paschen's law at short gap distances from 100 nm to 10 μm in air and nitrogen," Applied Physics Letters **105** (2014).
[33]G. Meng and Y. Cheng, "Electrical breakdown behaviors in microgaps," IntechOpen (2019).
[34]8600B, Agilent.
[35]Model 954, Fixed ratio single mode non-polarization maintaining fiber coupler, Evanescent Optics Inc.
[36]D. T. Smith, J. R. Pratt, and L. Howard, "A fiber-optic interferometer with subpicometer resolution for dc and low-frequency displacement measurement," Review of Scientific Instruments **80** (2009).
[37]J. Cripe, K. Arumugam, Y. Gerbig, and G. Shaw, "A static stiffness reference object for instrumented indentation with integrated fiber fabry–perot displacement measuring interferometer," Measurement Science and Technology **34**, 125032 (2023).
[38]J. R. Pratt, S. Schlamminger, F. Seifert, and D. B. Newell, "Verification of an in situ calibrated optomechanical accelerometer for use as a strong ground motion seismic reference," Metrologia **58**, 055005 (2021).
[39]D. Brouwer, J. Meijaard, and J. Jonker, "Large deflection stiffness analysis of parallel prismatic leaf-spring flexures," Precision Engineering **37**, 505–521 (2013).
[40]BOP HV, Kepco.
[41]J. L. Santos, A. P. Leite, and D. A. Jackson, "Optical fiber sensing with a low-finesse fabry–perot cavity," Appl. Opt. **31**, 7361–7366 (1992).
[42]APR001, Thorlabs inc.
[43]VP-25AA 25 mm travel motorized Actuator, and ESP 300 motion controller, Newport corporation.
[44]AV2, 50OO Durometer hardness, Thorlabs inc.
[45]TS140, The Table Stable ltd.
[46]731A, used at 1000V/g setting, Wilcoxon sensing technologies.
[47]2700A Andeen Hagerling.
[48]D.-K. Min and J. U. Jeon, "Analysis of the frequency response curve of a differential-type electrostatic actuator," 2nd ISA/IEEE Sensors for Industry Conference , 139–142 (2002).
[49]Tegam 2350 precision high voltage amplifier.
[50]XPR6U, Mettler Toledo.
[51]P. R. Wilkinson and J. R. Pratt, "Analytical model for low finesse, external cavity, fiber fabry–perot interferometers including multiple reflections and angular misalignment," Appl. Opt. **50**, 4671–4680 (2011).
[52]B. Poumellec, P. Guenot, R. Nadjo, B. Keita, and M. Nicolardot, "Information obtained from the surface profile of a cut single-mode fiber," Journal of Lightwave Technology **17**, 1357–1365 (1999).
[53]Y. Cheng, K. Sugioka, K. Midorikawa, M. Masuda, K. Toyoda, M. Kawachi, and K. Shihoyama, "Three-dimensional micro-optical components embedded in photosensitive glass by a femtosecond laser," Optics letters **28**, 1144–1146 (2003).
[54]C. Weingarten, S. Steenhusen, M. Hermans, E. Willenborg, and J. H. Schleifenbaum, "Laser polishing and 2pp structuring of inside microfluidic channels in fused silica," Microfluidics and Nanofluidics **21**, 1–9 (2017).
[55]F. He, Y. Cheng, L. Qiao, C. Wang, Z. Xu, K. Sugioka, K. Midorikawa, and J. Wu, "Two-photon fluorescence excitation with a microlens fabricated on the fused silica chip by femtosecond laser micromachining," Applied Physics Letters **96** (2010).
[56]R. Wagner, F. Guzman, A. Chijioke, G. K. Gulati, M. Keller, and G. Shaw, "Direct measurement of radiation pressure and circulating power inside a passive optical cavity," Opt. Express **26**, 23492–23506 (2018).
[57]P. A. Williams, J. A. Hadler, R. Lee, F. C. Maring, and J. H. Lehman, "Use of radiation pressure for measurement of high-power laser emission," Opt. Lett. **38**, 4248–4251 (2013).

[58] S. Vasilyan, M. López, N. Rogge, M. Pastuschek, H. Lecher, E. Manske, S. Kück, and T. Fröhlich, "Revisiting the limits of photon momentum based optical power measurement method, employing the case of multi-reflected laser beam," Metrologia **58**, 015006 (2021).

[59] R. Gates, W. Osborn, M. Mark McLean, G. Shaw, and J. Filliben, "Certification of standard reference material® 3461 reference cantilevers for afm spring constant calibration," **17**, 2852–2860 (2023).

IX. APPENDIX

A. Measurement of surface potential

In addition to the voltage applied to the electrodes, there is a surface potential, V_s, from contact potentials, patch effect and surface contaminants on the electrodes of the capacitor[1]. To evaluate V_s, voltage V_{DC} applied to the rod electrode was adjusted to produce the same force, determined by the interferometer signal, at positive and negative polarity, V_+ and V_-, respectively. Surface potential given by Eq. (22) is derived from Eq. (1). In the range of V_{DC} between -160 V and 160 V, it was found to be 0.4(1) V, where the uncertainty is the standard deviation of ten measurements.

$$V_s = \frac{(V_+^2) - (V_-^2)}{2((V_-) - (V_+))} = -\frac{(V_+) + (V_-)}{2} \tag{22}$$